Updating the pump and injector plate components of the ESPSS library in view of transient analysis of LOx/Methane engines

GLASGOW, SCOTLAND | 20-23 MAY 2024

Marco Fabiani[1], **Beatrice Latini**[2], **Francesco Nasuti**[3],
Chiara Boffa[4], **Mikhail Rudnykh**[5], **María Aranda Rosalez**[6], **Csaba Jeger**[7]

[1] Sapienza University of Rome, Rome, Italy, Email: m.fabiani@uniroma1.it
[2] Sapienza University of Rome, Rome, Italy, Email: beatrice.latini@uniroma1.it
[3] Sapienza University of Rome, Rome, Italy, Email: francesco.nasuti@uniroma1.it
[4] AVIO S.p.A., Colleferro, Italy, Email: chiara.boffa@avio.com
[5] AVIO S.p.A., Colleferro, Italy, Email: mikhail.rudnykh@avio.com
[6] Empresarios Agrupados Internacional S.A., Madrid, Spain, Email: maranda@empre.es
[7] ESTEC - European Space Agency, Noordwijk, The Netherlands, Email: csaba.jeger@esa.int

KEYWORDS: injectors, turbomachinery, low order modeling, LOX/LCH4

ABSTRACT:
This work summarizes some of the activities carried out by Sapienza University of Rome, Avio S.p.A. and Empresarios Agrupados Internacional in the framework of the EVACPRO project, an ESA funded activity aiming at improving EcosimPro/ESPSS capabilities, with a focus on transient simulations of LOX/LCH4 engines. The pump and injector plate components have been significantly improved. The injector pressure loss model has been updated to take into account the effects of injector geometry, swirl and distributed losses. A new thermal layout has been proposed, allowing for a better prediction of the injection plate temperature. The pump model has been extended to represent the most relevant fluid and thermal paths. A new thermal layout has been inserted, representative of the main thermal resistances and capacitances. The results of the proposed models have been compared with experimental data, showing promising results.

1. INTRODUCTION

As the space propulsion community is facing the challenges of a new space race, special care needs to be given to the improvement of engine design and analysis techniques, especially when novel concepts or propellants are considered. In particular, the role of reduced-order modeling techniques needs to be emphasized, especially during the preliminary design phases. In this context, the European space propulsion community benefits from the presence of the ESPSS toolkit, a common European platform for the design, analysis and simulation of space propulsion systems based on the EcosimPro framework, developed by ESA since 2006 [1].

This work summarizes some of the activities carried out by Sapienza University of Rome, Avio S.p.A. and Empresarios Agrupados Internacional (EAI) in the framework of the EVACPRO project (ESPSS Validation Activities for Chemical Propulsion Systems) , which is an ESA funded activity aiming at improving EcosimPro/ESPSS capabilities applied to transient simulations of complete chemical propulsion systems using novel propellants, with a particular focus on LOX/LCH4 engines [2]. In particular, the improvements on the injection plate and pump components are described here.

The injector plate is an engine system subcomponent which plays a central role on engine performances, stability and weight. A good injector plate should provide an efficient mixing dynamics, thus allowing for a chamber length reduction and for a decrease in the overall thrust chamber weight, in turn. The pressure loss induced by the injectors results, on one hand, on some protection against upstream pressure fluctuations, like, e.g., chugging instabilities, but results, on the other, on an higher pressure that the system has to deal with, upstream of the thrust chamber. For such reasons, the correct assessment of the pressure losses through the injector plate is a fundamental element to be considered during the design phase of an engine system. Moreover, an estimation of the injection plate temperatures during both engine start-up and steady-state operation is fundamental for the engine structural safety, since both convective and radiation heating of the injection plate may be non-negligible.

In high-pressure/high-thrust LREs, one employs pumps to bring the propellants at high pressure without the need for heavy pressurized tanks. In the framework of transient analysis, one must carefully model such components and their dynamics to obtain a faithful prediction of the engine start-up or shut-down. Moreover, when dealing with cryogenic propellants, such as LOX/LCH4, one has to take into account also the chilldown transient, needed to cool the pump before safely igniting the engine. Aim of the work presented here was to update the existing pump component, modeled as a single fluid volume, to model both the mechanical and thermal transients.

2. MODEL DESCRIPTION

2.1. Injector plate component

In this section the upgrades to the injection plate component have been summarized. Extensive description of all the models is available in the ESPSS user manual [3]. The new injector component, which is used inside the Preburner component (Fig. 1a) is represented by the symbol in Fig. 1b. New construction parameters have been added in order to select the injector and inlet types. Additionally, there is also the option to give the value of the pressure loss coefficient as an input given by the user. With respect to the injector of the previous release [4], three signal ports have been added, which allow to connect the injector to a propellant cavity and to another injector in order to exchange information if needed by the models (e.g., for the mixed injectors).

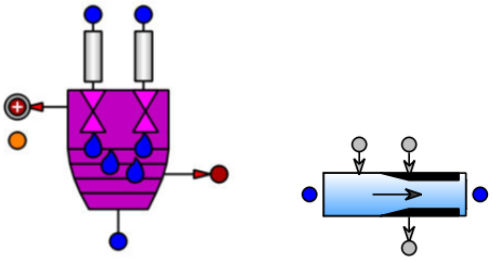

(a) Preburner component. (b) Injector component.

Figure 1: New components for injection plate modeling.

2.1.1 Mathematical Model for Pressure Losses

The injector pressure losses affect the flow through the momentum equation, which is written, in the 1-D model employed in the ESPSS libraries, as

$$I\dot{m} + \Delta p_{\text{loss}} = \Delta p \tag{1}$$

where I is the fluid inertia, $\dot{m}$ the mass flow rate and Δp the total-pressure difference between upstream and downstream of the injector. The pressure losses Δp_{loss} are computed as follows

$$\Delta p_{\text{loss}} = \frac{1}{2}\left(z + z_{\text{swirl}}\right)\left(\dot{m}/A\right)^2/\rho \tag{2}$$

Where z is the pressure loss coefficient and z_{swirl} is an additional loss coefficient used for swirl injectors. The limitation of the loss coefficient z for sonic flow has been retained from the previous ESPSS release. The friction factor z was before computed as with a sudden-contraction/sudden-expansion model, and can now be evaluated as function of both geometrical parameters and operating conditions for several injector types (Tab. 1).

Table 1: Injector types.

axial injectors			
single	mixed	perforated plate	
swirl injectors			
open	closed	bipropellant	gas

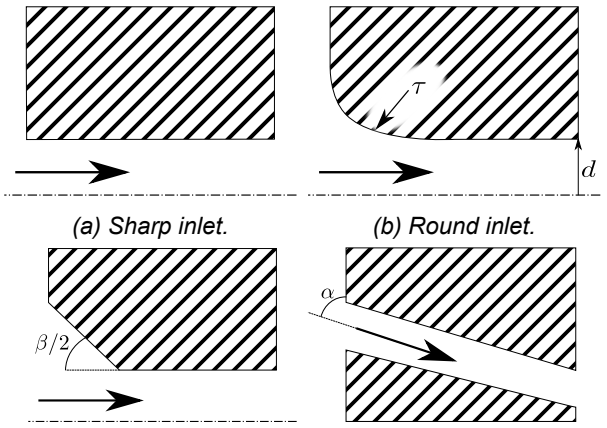

(a) Sharp inlet. (b) Round inlet.

(c) Slanted inlet. (d) Angled inlet.

Figure 2: Types of jet injector inlets.

Single jet injectors

The model described in this section is derived mainly from [5]. In the case of single jet injectors, namely injectors where the flow is axial and the propellants are not mixed together, the loss coefficient is computed as

$$z = z_{\text{inlet}} + z_{\text{Reynolds}} + z_{\text{friction}} + z_{\text{exit}} \tag{3}$$

- z_{Reynolds} takes into account the energy loss associated with the vortex generation when the liquid flows into the injector passage as function of the Reynolds number.
- z_{inlet} takes into account the effect of the sudden contraction at the injector inlet, as a function of the geometrical parameters of the injector. Four different inlet types are modeled: sharp (Fig. 2a), rounded (Fig. 2b), slanted (Fig. 2c) and angled (Fig. 2d).

  For the sharp inlet z_{inlet} is computed as:

$$z_{\text{inlet}} = 1/2\left(1 - A_o/A_1\right) \tag{4}$$

  where A_o is the orifice area and A_1 the upstream area, whereas, for the other inlet types, it is computed from tables obtained from [5]. Since such data are fitted for liquid flows, a correction coefficient has been introduced to take into account the effect of gas flows

$$z_{\text{inlet,gas}} = z_{\text{inlet}} c_{\text{gas}}, \quad c_{\text{gas}} = \left(1 - xD_o^2/D_1^2\right) \tag{5}$$

  where x is the vapour quality, D_o the orifice diameter and D_1 the upstream diameter.

- z_{friction} models the distributed losses inside the injectors due to friction and it is computed as

$$z_{\text{friction}} = f\, l/D_o \tag{6}$$

where f is the friction factor and l is the injector length.

- z_{exit} models the sudden expansion of the flow at the end of the injector. It is computed as

$$z_{\text{exit}} = (1 - A_o/A_2)^2 \tag{7}$$

where A_2 is the area of the component connected to the injector exit [6].

Mixed jet injectors

If mixed injector are used, namely injectors in which both liquid and gas flows are present (Fig. 3), z is computed as

$$z = z_{\text{inlet}} + z_{\text{mixed}} \tag{8}$$

where z_{inlet} is computed as shown above, and z_{mixed} is computed as a function of the ratio of the momentum flux between the two passages [5]. The new injector component is equipped with a signal port which carries the momentum flux information from one injector to the other one.

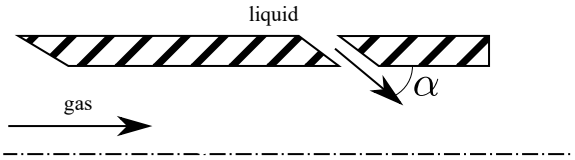

Figure 3: Mixed gas-liquid injectors.

Swirl Injectors

Concerning swirl injectors, the implemented models, taken from the available literature, first compute the discharge coefficient c_D, which is defined as

$$c_D = \frac{\dot{m}_{\text{real}}}{\dot{m}_{\text{ideal}}} \tag{9}$$

The discharge coefficient is linked to the pressure loss coefficient through the equation $z_{\text{swirl}} = 1/c_D^2$ and inserted in the pressure loss equation. Swirl injectors are characterized by high pressure losses, since the vortex motion leads to the formation of an open gas-filled core in the center of the liquid stream (Fig. 4).

Closed swirl injectors

For monopropellant closed-type swirl injectors (Fig. 4a) the semi-analytical model of Bazarov [5] has been implemented. Each swirl injector is characterized by its Swirl Number (SN), which is a non-dimensional quantity representing the rotational intensity of the flow. From the knowledge of the geometrical characteristics of the injector (see Fig. 4) an

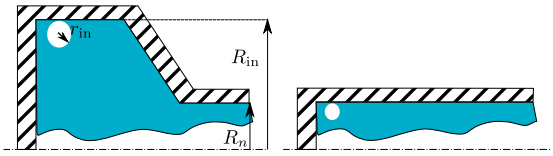

(a) Closed type. *(b) Open type.*

Figure 4: Monopropellant swirl injectors.

"equivalent swirl number" SN_{eq} may be evaluated:

$$SN_{\text{eq}} = \frac{R_{\text{in}} R_n}{n r_{\text{in}}^2 + \frac{\lambda}{2} R_{\text{in}} (R_{\text{in}} - R_n)} \tag{10}$$

where

$$\lambda = 0.3164/Re^{0.25}$$

From the equivalent swirl number SN_{eq} the coefficient of fullness ϕ (which represents the ratio between the cross section filled by the liquid and the overall cross section) may be evaluated solving

$$SN_{\text{eq}} = \frac{(1-\phi)\sqrt{2}}{\phi\sqrt{\phi}} \tag{11}$$

and the discharge coefficient is computed as

$$c_D = \frac{c_{D,\text{eq}}}{\sqrt{1 + z c_{D,\text{eq}}^2 \frac{SN^2}{\bar{R}_{\text{in}}^2}}}, \quad c_{D,\text{eq}} = \frac{\phi\sqrt{\phi}}{\sqrt{2-\phi}} \tag{12}$$

where $SN = \frac{A_n R_{\text{in}}}{A_{\text{in}} R_n}$ is the swirl number of the injector and $\bar{R}_{\text{in}}$ is the radial location of the center of the inlet passage divided by the injector exit radius R_n. The standard pressure loss coefficient is evaluated as

$$z = z_{\text{inlet}} + \lambda \frac{l_{\text{in}}}{D_{\text{in}}}$$

where z_{inlet} is the same coefficient as in the above sections. The discharge coefficient is then expressed as an additional pressure loss term due to the rotational motion, $z_{\text{swirl}} = 1/c_D^2$.

Open swirl injectors

For the open-type swirl injectors (Fig. 4b) the empirical correlation of [7] has been implemented. The discharge coefficient is computed as

$$c_D = 0.19 \left(A_n/D_o^2\right)^{0.65} \beta^{-2.13} \tag{13}$$

where A_n is the exit area of the injector and $\beta = D_{in}/D_n$.

Bipropellant swirl injectors

For bipropellant swirl injectors, namely swirl injectors in which the oxidizer and fuel flow interact in some way (Fig. 5) different cases must be analyzed. The adopted modeling technique follows [5].

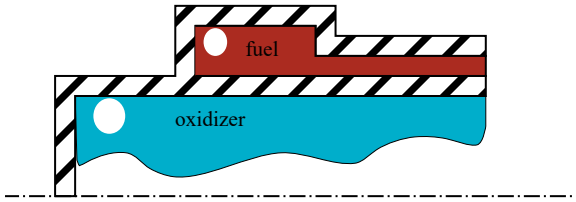

(a) External mixing.

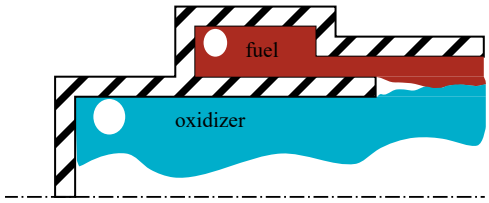

(b) Internal mixing.

Figure 5: Bipropellant swirl injectors.

- Injectors with external mixing. In this case (Fig. 5a) the mixing of the two liquid streams happens outside of the injector. The discharge coefficient of the inner injector can be computed as for a monopropellant one. The pressure loss of the external injector can be computed as in the previous sections only if the nozzle of the internal stage is designed to be accommodated in the gas core of the external injector, namely the two injectors are hydraulically independent. If this is not the case, the discharge coefficient is computed employing the data of [5].
- Injectors with internal mixing (Fig. 5b). Here the mixing of the liquid streams starts inside the injector. The discharge coefficient of the inner injector can be computed as for a monopropellant injector, while the discharge coefficient of the outer injector is usually over-predicted by the models of Sec. 2.1.1 and 2.1.1. No model has been implemented for this specific case, due to the dependace of the pressure loss on the specific geometry of the injector. Correlations such as the ones of [7] may be used.

Gas-swirl injectors

For gas-swirl injectors the discharge coefficient is computed from the data of [5], fitted in the following laws

$$\begin{aligned} c_D &= c_{D,ref}\bar{c_D} \\ \bar{c_D} &= 1 + (0.246(R_{in}/R_n) - 0.1885)SN \\ c_{D,ref} &= 0.08\varepsilon + 0.01 + \exp(-1.15SN) \end{aligned} \quad (14)$$

where ε is the expansion ratio of the injector' nozzle. $c_{D,ref}$ is the discharge coefficient for $R_{in}/R_n = 0.75$ and $\bar{c_D}$ is a correction factor.

Perforated plate

A perforated-plate model has been inserted, based on the data reported in [6]. Several expressions

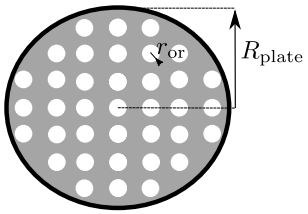

Figure 6: Schematics of perforated plate.

have been implemented to compute the pressure loss coefficient as a function of the geometry, of the Reynolds number and of the plate porosity f, defined as (Fig. 6)

$$f = \frac{n\pi R_{or}^2}{\pi R_{\text{plate}}^2} \quad (15)$$

where n is the number of orifices in the plate, R_{or} the orifice radius and R_{plate} the plate radius. The implemented models allow to take into account both thick and thin plates, with sharp, round or slanted inlets.

2.1.2 Mathematical Model for Heat Transfer

The modelling of heat transfer towards the injector plate is a matter much less treated than the one for instance in the nozzle of rocket engines [5], mainly due to the complexity of the flow field in the injection zone [8]. Furthermore, the lack of experimental data, due to the difficulty in inserting thermocouples in the injector head, limits the validation cases of any simplified model. Few examples are present in literature, such as [9] and [10]. The only simplified models present in literature are the ones already implemented in the EcosimPro/ESPSS framework [4, 11].

Looking at commonly used injection plates geometries (Fig. 7), it appears appropriate to model the injector plate as a cluster of walls connected to the chamber and the oxidizer and fuel domes. Thermal resistances are employed to model the walls, and a "series" approach is employed (Fig. 9), while the previous models adopted a "parallel" approach (Fig. 8). Such arrangement of resistances is preferred since the oxidizer and fuel domes are usually one on top of the other.

The computation of the heat flux towards the injectors is performed as in the previous release (ESPSS 3.6 [4]).

For each wall crossed by the injection channels (walls 1, 2 and 3), an additional forced convection term has been computed

$$q_{\text{conv}} = A_{\text{wet}} h_{\text{conv}} (T_{\text{wall}} - T_{\text{fluid}}) \quad (16)$$

where A_{wet} is the lateral surface of the injection channels and h_{conv} the heat transfer coefficient (computed with the Dittus Boelter equation). All fluid properties are taken in the upstream cavity. The computed heat flux q_{conv} is imposed at the nodes.

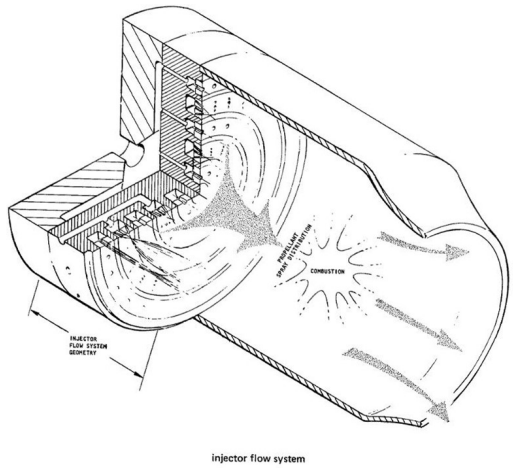

Figure 7: F1 rocket engine injection plate [8].

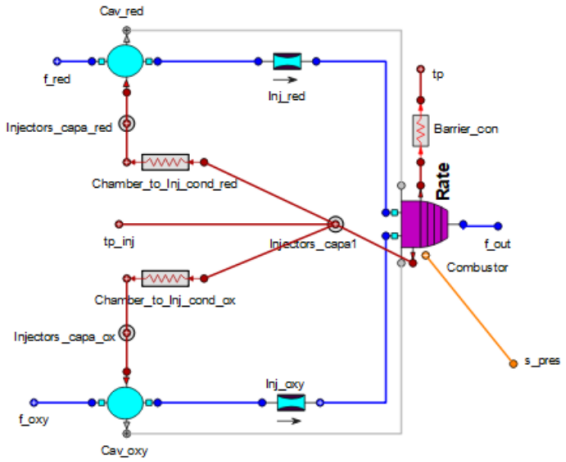

Figure 8: Injection plate schematics in ESPSS 3.6 [4].

2.2. Pump component

In this section the pump component is described. Aim of the work was to identify a component topology which could be able to correctly represent both the mechanical and thermal transients of cryogenic LRE pumps.

Comparing literature data such as [12] and the main characteristics of cryogenic pumps now in use, a network model, inspired by the one shown in Fig. 10, is built using the components already available in the Ecosimpro/ESPSS framework. Such kind of approach is expected to be computationally lightweight and versatile. The original pump model is used as a starting point to develop the enhanced one, retaining the map-based modeling for the pump pressure rise. In addition, the two flows running through both the main pump channel and the secondary interstices, are specifically modeled. Those channels are connected to mass elements which are representative of the solid pump parts, allowing for a detailed thermal analysis. Such approach should allow for both retaining a reasonable computational speed and fulfil the capability of simulating the chill-down process, the transient and the operative regimes, within the same numerical model.

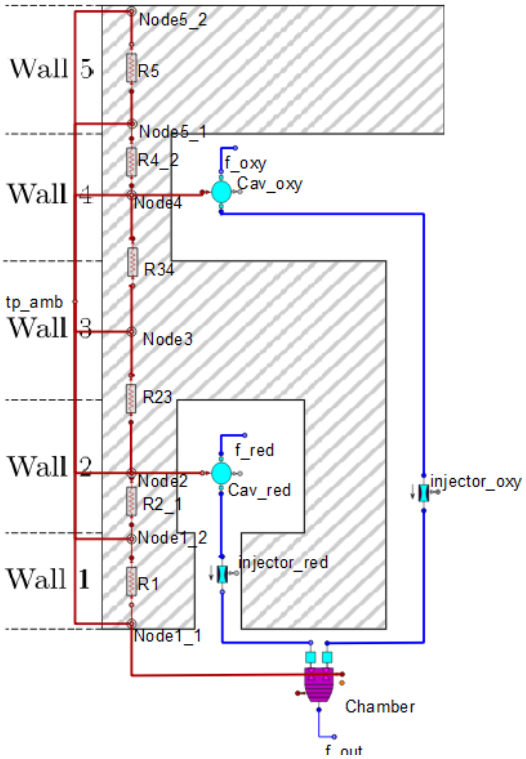

Figure 9: Injection plate thermal network.

As shown in Fig. 10, the flow splits towards two directions, i.e., the low resistance-main pump channel and the high resistance-bearings interstices. Such split dynamics is ruled by two tunable concentrated losses, allowing the user to calibrate their model on the basis on the actual hardware hydraulic resistance. Default and approximated loss values might be provided on the basis of the validation outcomes.

From a thermal point of view, heat exchange with ambient and also between the two lines is included. A user tunable bearings-generated heat is enforced at the related thermal node.

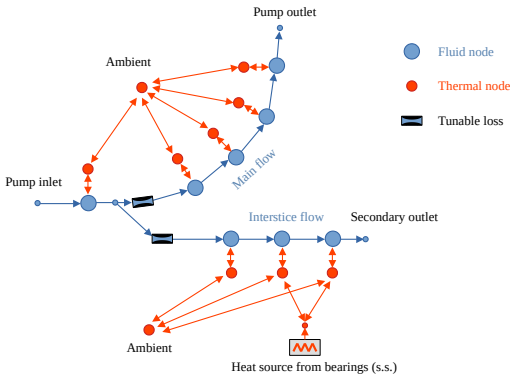

Figure 10: Sketch of the new pump component inner structure.

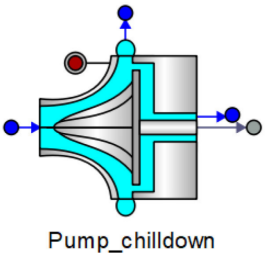

Figure 11: Newly developed pump component symbol.

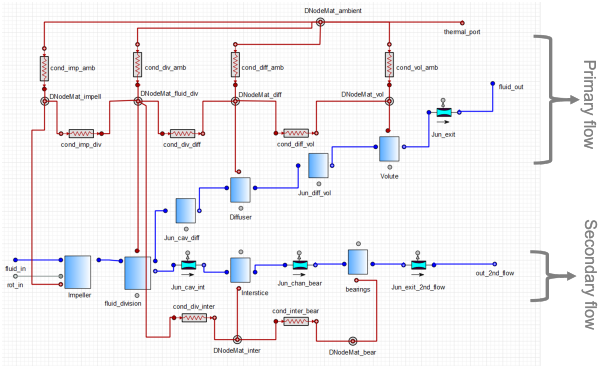

Figure 12: Component layout.

Finally, a minor modification has been added to the mechanical balance equation to take into account the start-up torque of the pump.

3. VALIDATION

In this section the results obtained in the validation of the implemented models are reported. The validation has been performed taking into account both test cases reported in the open literature and experimental data obtained by AVIO S.p.A.

3.1. Injector pressure losses

3.1.1 Validation on literature data

A preliminary validation of the implemented models has been performed comparing the results obtained with EcosimPro with available literature data on jet injectors, swirl injectors and perforated plate. Due to the lack of accurate data on actual rocket injectors, the validation has been performed on laboratory cold-flow tests, with water as fluid. The schematic employed is shown in Fig. 13.

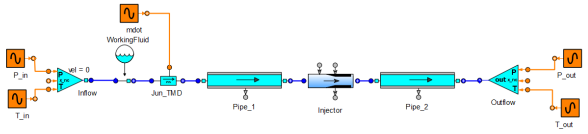

Figure 13: Schematics employed for preliminary validation of pressure loss model.

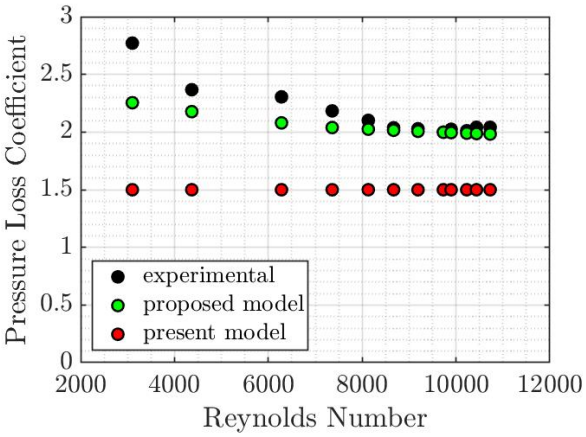

(a) Sharp inlet injector.

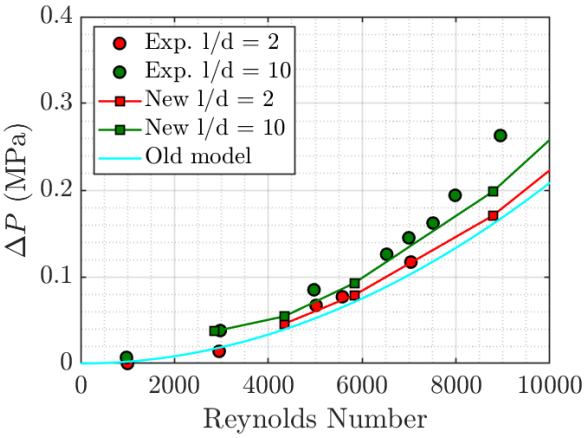

(b) Sharp inlet injector.

Figure 14: Validation results for jet injectors.

The mass flow rate is imposed through a JUN TMD component, in order to match the experimental mass flow rate. The pressure and temperatures are set to match the experimental conditions. Two pipes have been inserted before and after the orifice, to simulate the entire test section and properly connect the injector to the boundary condition.

The selected test cases allowed to evaluate the performance of the models on jet injectors with sharp [13] and slanted [14] inlets, on open and closed swirl injectors [7] and on perforated plates [15]. The results in terms of pressure loss or pressure loss coefficient are reported in Figs. 14a, 14b and 15.

All cases show a significant improvement from the current model (ESPSS 3.6 [4]) to the proposed one, which is able to capture all the main dependencies of the pressure loss. Fig. 14a shows the effect of the introduced dependence of ζ on Re, which however deviates from the experimental data at low Reynolds numbers. This effect may be due to the friction correlations which might underestimate the friction factor at low-flow conditions. Fig. 14b shows instead how the model is able to capture the dependence of the pressure loss on the main geometrical parameters of axial injectors. The results on swirl injectors (Fig. 15) and perforated plates (Fig. 16) show ex-

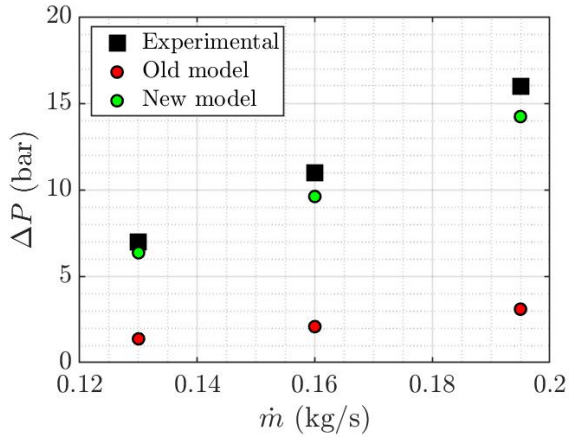

(a) Closed injector.

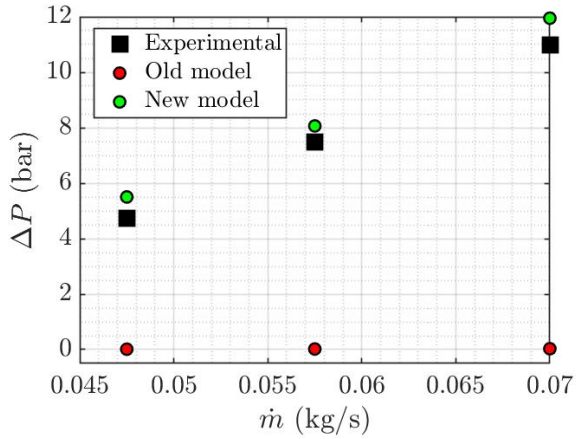

(b) Open injector.

Figure 15: Validation results for swirl injectors.

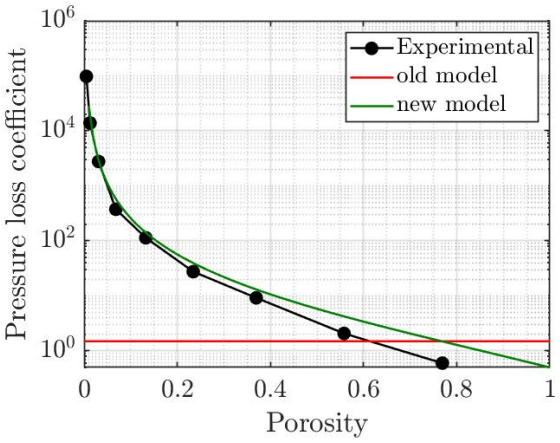

Figure 16: Validation results for perforated plate.

tremely satisfactory results, especially given that the previous models could not take into account such configurations.

3.1.2 Validation on AVIO data

The proposed numerical models have been validated against experimental data available at AVIO. The models for pressure losses in injectors have been validated against two sets of experimental data, which has allowed to rely on a larger set of experimental data and to perform adequate validation of the models. In particular, numerical experiments have been performed considering: - water as working fluid, with the scope to replicate the setup of cold-flow tests performed at AVIO; - LOX as working fluid, with the scope to replicate the setup of hot-firing tests performed at AVIO. In all the tests the Reynolds number was larger than 12000, and hence these allowed to further extend the validation performed preliminary by University of Rome "La Sapienza". In Fig. 17 is shown the schematic considered for the analyses on injectors.

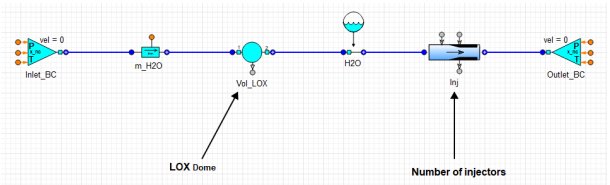

Figure 17: AVIO schematics employed for validation of injector models.

A set of analyses have been performed, in order to assess the performance of the proposed models at increasing Reynolds number. In particular, following models have been investigated, since these are considered more applicable to the design of the hardware:

- jet injector, with sharp edges;
- jet injector, with rounded inlet;
- jet injector, with slanted inlets;
- perforated plate.

For each of the above models, five simulations were performed considering different mass flow rates at inlet, which correspond to increasing Reynolds number. Results at steady state are shown in following Fig. 18. As expected, for given Reynolds number the contraction-expansion provides the largest pressure drop through injectors. The use of models with rounded or slanted inlets produces lower dP, and adjustment of the β angle does not produce appreciable differences in the results. Finally, the model of perforated plate (in grey) produces the lowest pressure drop and it allows to better reproduce the experimental data (in yellow).

As shown in Tab.2, the percentage error on the pressure at injector inlet predicted at increasing mass flow rates is significantly lower for the perforated plate model, typically not higher than 32% at the highest value of Reynolds number.

Numerical experiments have been performed with the aim to replicate the conditions of hot firing tests. In this case, the comparison with experimental data have shown even better agreement with available data, with numerical error lower than 10% over the

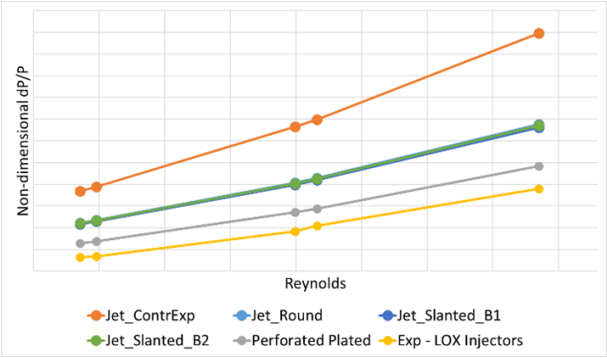

Figure 18: Steady state results.

entire range of mass flow rates investigated, see Tab.3. This is probably due to the increased accuracy of the sensors used for the hot firing tests.

Table 2: Percentage error wrt experimental data – cold flow tests.

Test	contraction-expansion	perforated plate
1	137	18.9
2	141	21.6
3	150.3	26.4
4	157.3	33
5	153	31.6

Table 3: Percentage error wrt experimental data – hot firing tests.

Test	perforated plate model
1	0.38
2	1.67
3	4.46
4	6.34
5	9.14
6	9.96

3.2. Injection plate heat transfer

3.2.1 Validation on literature data

A preliminary validation of the adopted model has been performed on the experimental data reported in [10]. The experiment consists on a H_2-O_2 combustion chamber, operating at $O/F = 2.9$ and $\dot{m} = 1.52$ kg/s at 55 bar. Being the chamber sink-cooled the test duration is significantly short and steady state conditions are never reached. The schematics employed for the simulations, shown in Fig. 19, has been taken from the Preburner-Test schematic of the ROCKET_EXAMPLES library and modified with the addition of the the new preburner component. An ambient node with imposed temperature with exchanges by convection and radiation with the injection plate has also been added. The relevant inputs have been extrapolated from the experiment and are reported in Fig. 20.

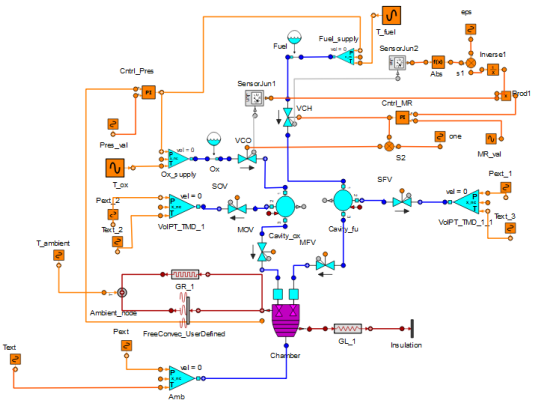

Figure 19: Schematics employed for preliminary validation of pressure loss model.

cond_inj	391.1	W/(m-K)	Injector thermal conductivity if material is None
capa_inj	393.5	J/(kg-K)	Injector specific heat capacity if material is None
mass_inj1	0.566	kg	mass - Node 1
mass_inj2	0.506	kg	mass - Node 2
mass_inj3	0.158	kg	mass - Node 3
mass_inj4	0.692	kg	mass - Node 4
mass_inj5	0.247	kg	mass - Node 5
S_cond1	0.0124	m^2	conducting surface - R1
S_cond2	0.0124	m^2	conducting surface - R2
S_cond3	0.0124	m^2	conducting surface - R3
S_cond4	9.02E-3	m^2	conducting surface - R4
S_cond5	9.02E-3	m^2	conducting surface - R5
th_inj1	0.051	m	wall thickness - R1
th_inj2	0.0456	m	wall thickness - R2
th_inj3	0.0143	m	wall thickness - R3
th_inj4	0.0858	m	wall thickness - R4
th_inj5	0.0306	m	wall thickness - R5

Figure 20: Experiment inputs.

As shown in Fig. 21a, the proposed model appears to be able to represent the heating transient of the injection plate within a significantly low error threshold. However, during the cooling transient the level of agreement of the numerical solution appears lower, and that is due to the uncertainties in the test shutdown sequence, which is not reported in the paper.

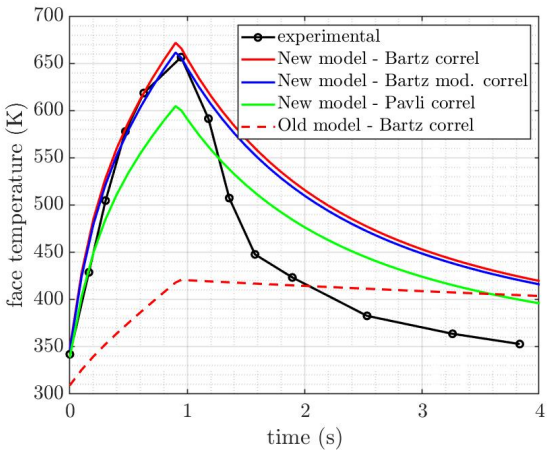

(a) Results without forced convection in the injection channels.

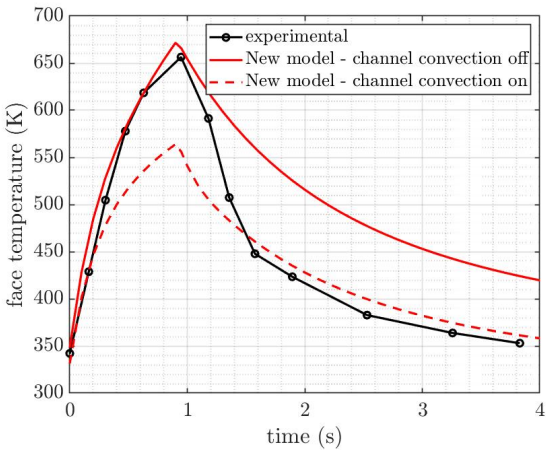

(b) Results with forced convection in the injection channels.

Figure 21: Preliminary validation of thermal model of the injection plate.

Fig. 21a is obtained without considering convective heat transfer inside the injection elements. If the convection is considered, (see Fig. 21b) the maximum temperature is underestimated. For this reason, and because of the simplicity of the convective heat transfer model within the elements, the convective term has been set as optional, in the component.

Since it seems that the temperature decrease phase is better fitted by the model employing the convective term, it has to be pointed out that such a phase does not change among the two tests because the engine shutdown is operated completely closing the propellant valves in both cases.

3.2.2 Validation on AVIO data

Similarly, the validation of implemented thermal model has been performed considering the schematic shown in Fig.22.

The actual geometrical characteristics of the hardware as well as appropriate material properties have been implemented. In Figs.23 and 24 below is shown, as an example, the comparison between numerical results and experimental data (in blue) in terms of both LOX and solid temperature of the LOX dome as function of non-dimensional time. Similar results have been derived also for the CH4 side.

As shown in Fig. 23, the model appropriately reproduces the experimental data in terms of fluidic temperature. On the other side, the solid temperatures are not well reproduced during transient and at steady state. This might be due to the effective thermal conductivity of the component and to the actual exposed surfaces for the heat exchange between the fluid and the solid. In fact, the numerical model implies important simplification of the hardware and it does not allow to model in details all the actual contact points and interstices. Moreover, although sensors were placed on the external surfaces of LOX dome and CH4 manifold, these were at axial location which cannot be directly linked one-

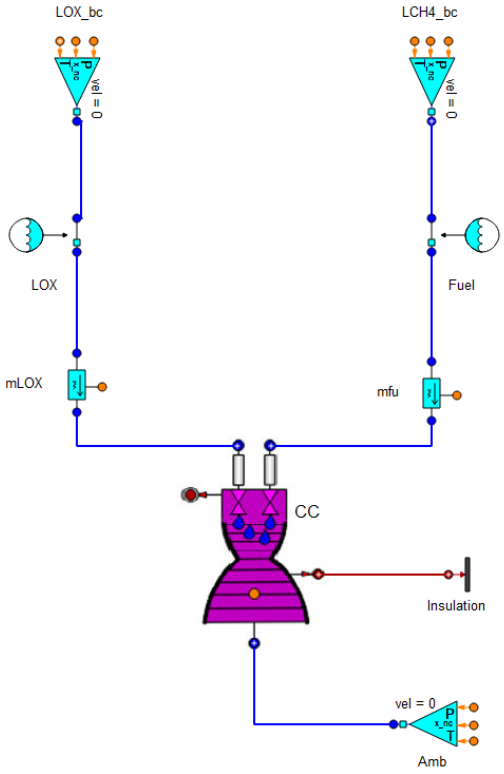

Figure 22: AVIO schematic employed for the thermal model validation.

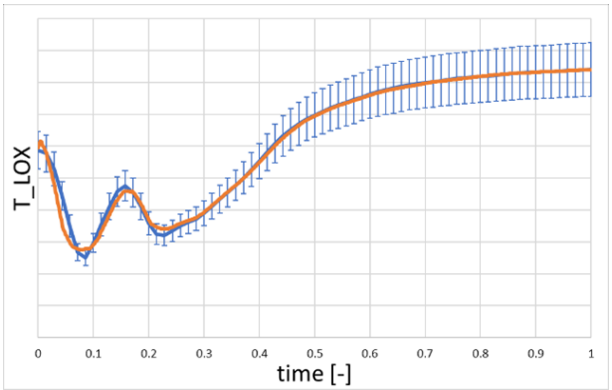

Figure 23: LOX temperature in injector dome.

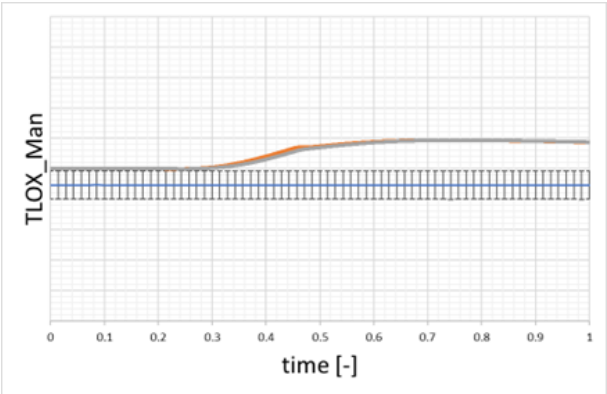

Figure 24: Solid temperature of the LOX dome.

to-one to the available numerical nodes. However, the component in ESPSS allows for appropriate tuning of the model and different values of the exposed surfaces and thermophysical properties of the solids based on customer statistical data.

3.3. Pump thermal behaviour

3.3.1 Validation on literature data

Fig. 25 shows the schematic used for the validation. The experiment consists on a static pump chilldown, controlled by cavity outlet passage of 4mm diameter, represented by a Junction, using LOX at 85 K. Both the primary and the secondary flows are then discharged through two separate combustion chambers, in order to define robust boundary conditions, since the main goal of this test is to simulate the behaviour of the internal components of the pump. The input data are reported in Tab. 4.

Table 4: Input data used for the preliminary validation.

Variable	Value
T_o	293.15 K
qi_bearings	200 W
cp	600 J/(kg K)
cond	10 W/K
zetaf_interstice	1000000
zetab_interstice	1000000
mass_impeller	1.95 kg
mass_fluid_division	1.95 kg
mass_diffuser	1.95 kg
mass_volute	1.95 kg
mass_interstice	1.95 kg
mass_bearings	2.25 kg

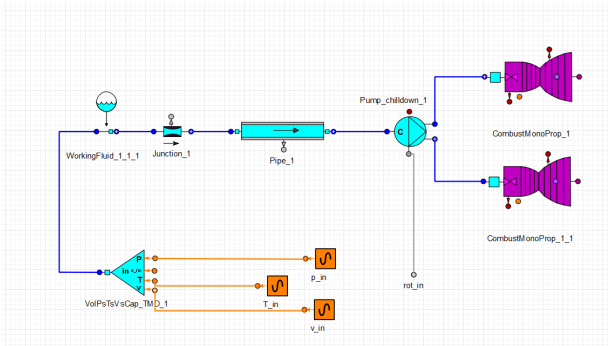

Figure 25: EcosimPro schematic of the experiment used for the preliminary validation.

Fig. 26 shows a comparison of experimental data with EcosimPro simulations. In particular, numerical simulations are performed both considering and neglecting an additional heat generated by the bearings. The level of agreement between the numerical and experimental data is significant. However, it must be pointed out that the inner pump masses were not available in the paper and thus they have been reconstructed to fit the data. Nevertheless, the two appearing inflection points characterizing the chilldown process of the experiment are well reproduced by the newly developed component. Such behavior is an indication of a potential good reliability of the implemented model.

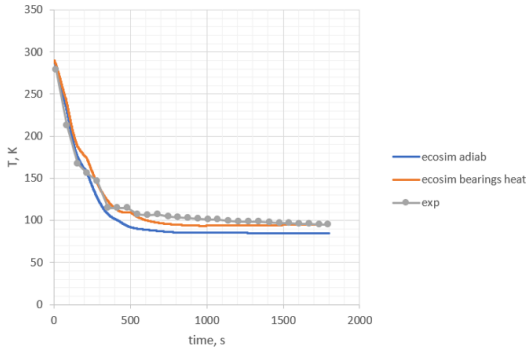

Figure 26: Preliminary validation of the pump component.

3.3.2 Validation on AVIO data

Numerical analyses have been performed in order to validate the new developed pump model. In particular, analyses have been focused on the assessment of the performance of the model during chilldown phase and during start-up transient. On the basis of the schematic representation proposed by University of Rome La Sapienza, AVIO has identified model observables and these have been linked to specific sensors installed on the hardware, including both fluidic and temperature sensors as well as pressure sensors. Unfortunately, not all numerical nodes could be linked to experimental observables due to the absence of sensors in the specific positions. Several simulations have been performed, considering both LOX and LCH4 pumps and with the scope to assess the influence of the models for heat exchange between the fluid and the solid walls of the tube components: `HT_Boiling` and `HT_Tube`, which are considered the most promising.

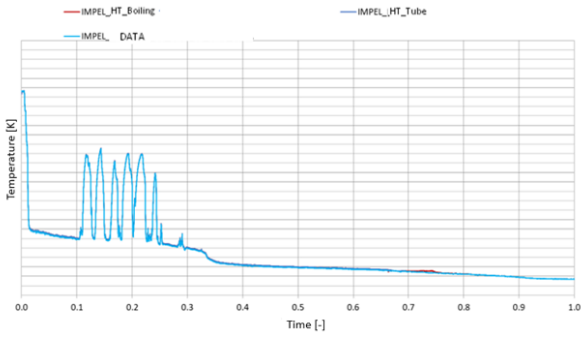

Figure 27: Impeller temperature profile.

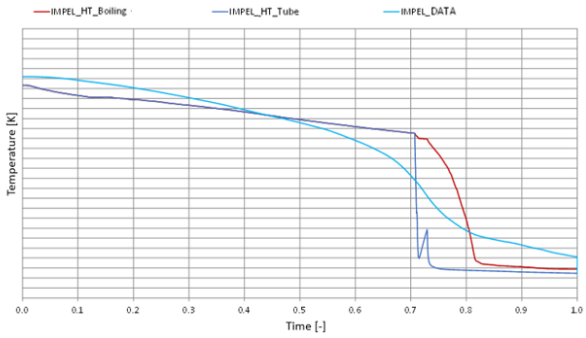

Figure 28: DNODE MAT IMPELL temperature profile.

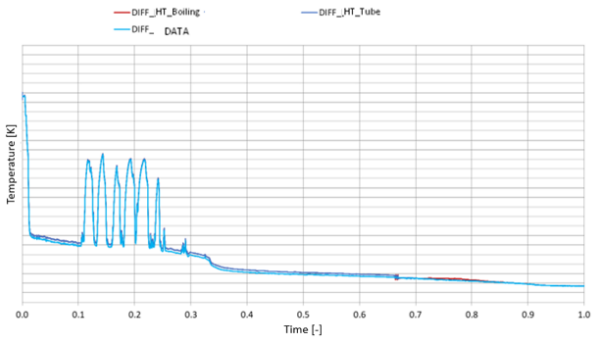

Figure 29: Diffuser temperature profile.

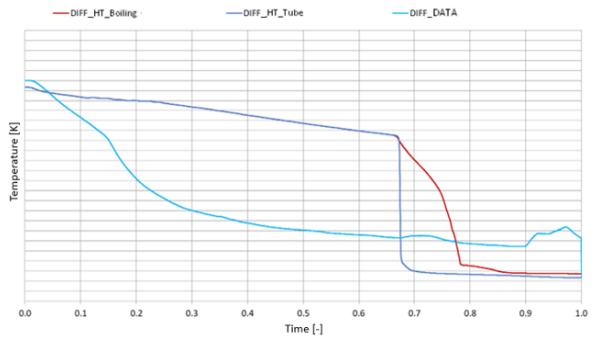

Figure 30: DNODE MAT DIFF temperature profile.

As also experienced for the thermal models for injectors, the fluidic temperatures are typically well reproduced, however the solid temperatures are usually not well predicted. As an example, in Figures 27 to 30 are shown the temperature profiles of the fluid and of the solid node of the impeller component and of the diffuser, for which experimental data from temperature sensors were available. As shown, the numerical model provides more accurate predictions of the fluidic temperatures rather than of the solids during the chill-down phase. In both cases, the model considered for the fluid-solid heat exchange in the tubes does not produce major impact on the numerical results. This result can be easily justified considering that the internal layout of a pump is very complex, and an accurate description of the flow path and of the heat exchange between the fluid and the exposed solid surfaces is very complex. However, the activity has highlighted that the model can be useful during the design process to get an overall assessment of the fluid consumption during the chill-down phase, which has been fairly predicted.

4. CONCLUSIONS

In this work some of the advancements carried out in LOX/LCH4 rocket engine modeling in the framework of the EVACPRO project have been described. The activities allowed to implement and validate low-order models for the modeling of heat transfer and pressure loss in injection plates and of the thermal behaviour of cryogenic pumps. Validation on both literature and AVIO experimental data showed how the proposed models allow for a significant improvement in the predictive capabilities of the ECOSIMPRO/ESPSS tool. The injector pressure loss showed good results on both cold-flow test cases taken from the open literature and hot firing tests performed by AVIO. The results obtained on the pump chilldown showed how it is possible to obtain a good match between numerical and experimental data even with low-order models, but that, due to the complexity of the systems, a direct match between measured and computed observables is not always present.

References

[1] J. Steelant, M. De Rosa, J. Moral, and R. Pèrez. Espss simulation platform. *Space Propulsion Conference*, 2010.

[2] F. Rodriguez, F. Nasuti, K. Wroblewski, C. Boffa, B. Hammerli, , and C. Jeger. Improving liquid propulsion modeling capabilities in the european space propulsion system simulation (espss) library. *2nd International Conference on Flight Vehicles, Aerothermodynamics and Re-entry Missions Engineering (FAR)*, 2022.

[3] *ESPSS EcosimPro Libraries User Manual 3.7.0*, 2024.

[4] *ESPSS EcosimPro Libraries User Manual 3.6.0*, 2022.

[5] V. G. Bazarov. Design and dynamics of jet and swirl injectors. In Yang and Habiballah, editors, *Liquid Rocket Thrust Chambers*, pages 19–103, 2004.

[6] I. E. Idelchik and E. Fried. Handbook of hydraulic resistance: Second edition. 1986.

[7] K. Ahn and B. J. Lee. Experimental study on the discharge coefficient of bi-swirl coaxial injectors. *Journal of Applied Fluid Mechanics*, 12:1439–1447, 09 2019.

[8] G.S. Gill and W. H. Nurick. *NASA SP-8089:Liquid rocket engine injectors*, 1976.

[9] J. Pichillou, P. Grenard, L. Vingert, G. Leplat, and P. Reulet. Experimental analysis of heat transfer in cryogeniccombustion chambers on Mascotte test bench. *EUCASS*, 2017.

[10] M. A. deRidder and W. E. Anderson. Heat flux and pressure profiles in an oxygen/hydrogen multielement rocket combustor. *Journal of Propulsion and Power*, 26(4):696–705, 2010.

[11] F. Di Matteo, M. De Rosa, and M. Onofri. Semi-empirical heat transfer correlations in combustion chambers for transient system modelling. 2010.

[12] J. Joseph, G. Agrawal, D. K. Agarwal, J.C. Pisharady, and S. S. Kumar. Chilldown study of cryogenic turbopump bearing coolant cavity. *ICAME*, 2015.

[13] K. Ramamurthi and K. Nandakumar. Characteristics of flow through small sharp-edged cylindrical orifices. *Flow Measurement and Instrumentation*, 10(3):133–143, 1999.

[14] D.N. Kiaoulias, T.A. Travis, J.D. Moore, and G.A. Risha. Evaluation of orifice inlet geometries on single liquid injectors through cold-flow experiments. *Experimental Thermal and Fluid Science*, 103:78–88, 2019.

[15] S. Malavasi, G. Messa, U. Fratino, and A. Pagano. On the pressure losses through perforated plates. *Flow Measurement and Instrumentation*, 28:57–66, 2012.